ACS OMEGA

http://pubs.acs.org/journal/acsodf

Article

Miniaturized Control of Acidity in Multiplexed Microreactors

Divya Balakrishnan, Janwa El Maiss, Wouter Olthuis, and César Pascual García*

Cite This: *ACS Omega* 2023, 8, 7587−7594

Read Online

ACCESS | Metrics & More | Article Recommendations | Supporting Information

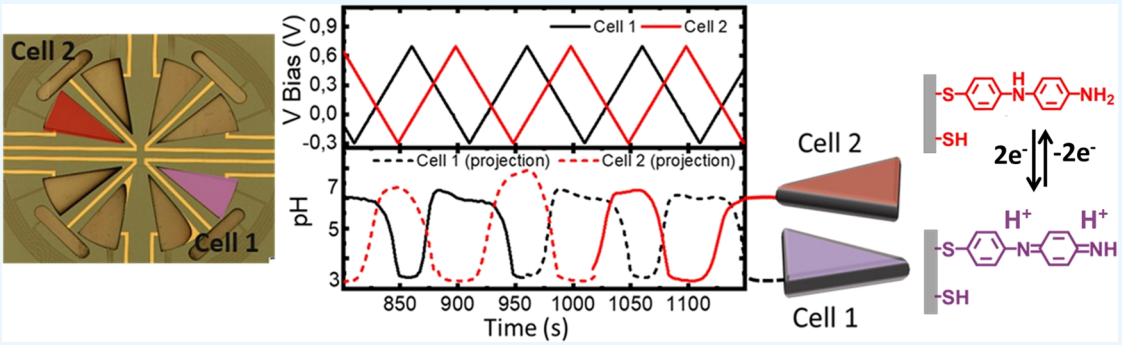

ABSTRACT: The control of acidity drives the assembly of biopolymers that are essential for a wide range of applications. Its miniaturization can increase the speed and the possibilities of combinatorial throughput for their manipulation, similar to the way that the miniaturization of transistors allows logical operations in microelectronics with a high throughput. Here, we present a device containing multiplexed microreactors, each one enabling independent electrochemical control of acidity in ∼2.5 nL volumes, with a large acidity range from pH 3 to 7 and an accuracy of at least 0.4 pH units. The attained pH within each microreactor (with footprints of ∼0.3 mm^2 for each spot) was kept constant for long retention times (∼10 min) and over repeated cycles of >100. The acidity is driven by redox proton exchange reactions, which can be driven at different rates influencing the efficiency of the device in order to achieve more charge exchange (larger acidity range) or better reversibility. The achieved performance in acidity control, miniaturization, and the possibility to multiplex paves the way for the control of combinatorial chemistry through pH- and acidity-controlled reactions.

1. INTRODUCTION

Acidity is a parameter that can drive chemical reactions, and its control is one of the most important strategies in processes such as the assembly of DNA,[1−4] the control of polymer structures,[5,6] or the solid-phase synthesis of biopolymers like peptides,[7] nucleotides,[8] and saccharides,[9] which form the foundation of combinatorial chemistry. The miniaturized control of these reactions has several advantages: (a) an increase in the kinetics by reducing the distance between the molecules, (b) the possibility to increase the number of simultaneous reactions providing a multiplexed control to achieve high combinatorial throughput with high-density arrays, and (c) reduction of consumption of reagents, minimizing the costs of production. Solid-phase synthesis also facilitates the miniaturization of chemical reactions controlled by acidity, delivering reagents and allowing the immobilization of the product molecules into addressable substrate regions by applying a tailored acid treatment into each different spot.[10,11] On the other hand, the local control of acidity enables the introduction of reagents in parallel that will react depending on the acid treatment to multiplex the chemical reactions. This strategy greatly decreases the time to produce microarrays. A successful proof to this was shown by Price and co-workers,[12] who used photogenerated acid by molecules that were introduced into a spin-casted photosensitive resist. With this method, they made arrays with spots of area 50 × 50 μm^2. A similar method was reported with an array of reactors that used photogenerators of acid immobilized with other reagents in the reactor volumes for the synthesis of DNA.[13] Here, the generated acid was confined in the space of the reactor volume and the photogenerating molecules were flushed into the reactors for every chemical reaction. Photoactive molecules were also used to release OH^- ions to alter the pH to basic conditions, while controlling the enzymatic reactions on DNA.[14] Though the photoactivated processes have shown that they can drive reactions under acidic and basic conditions in a miniaturized size, they require more cumbersome equipment and processes since they have to combine microfluidics and optical microarrays.

Received: November 2, 2022
Accepted: January 23, 2023
Published: February 17, 2023

https://doi.org/10.1021/acsomega.2c06897
ACS Omega 2023, 8, 7587−7594

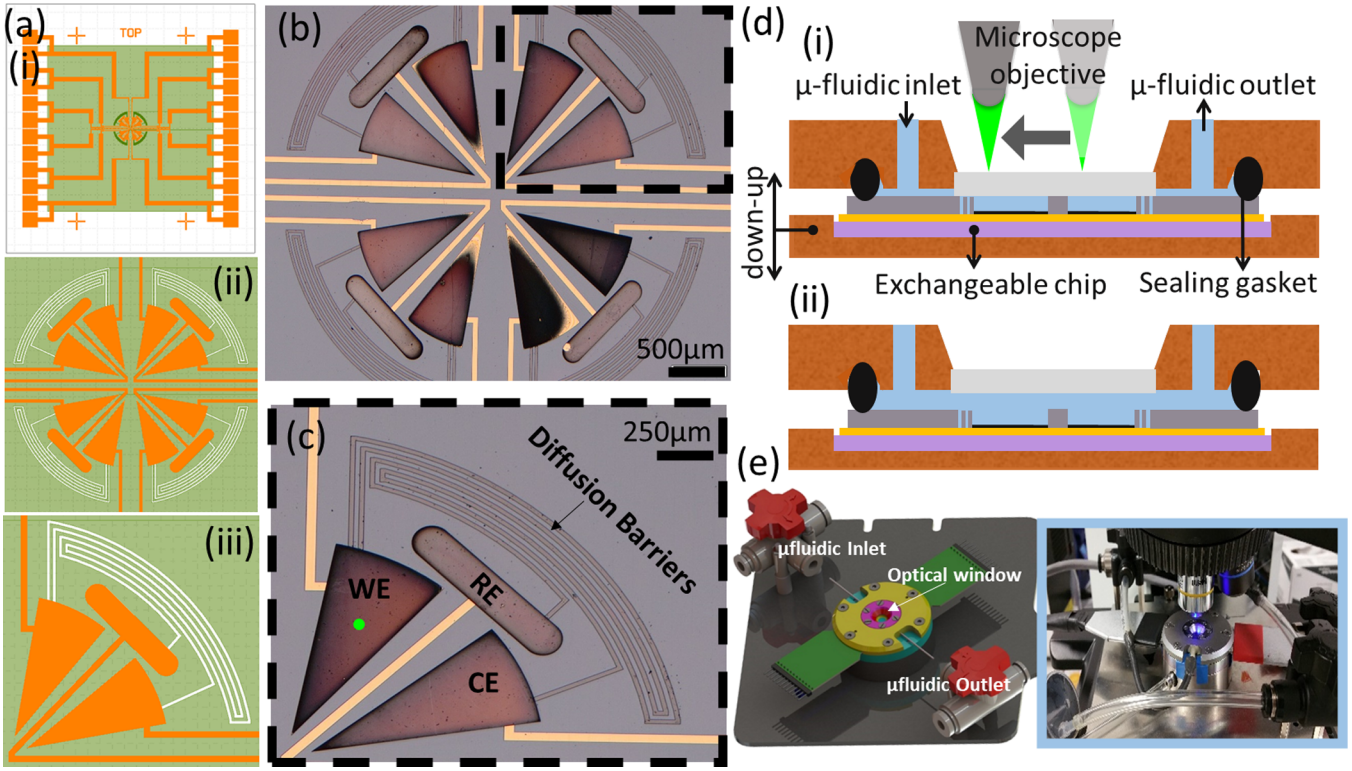

Figure 1. (a) CAD designs of (i) the full chip, (ii) enlarged view of the four microreactors, and (iii) enlarged view of one microreactor. (b) Microscopy image of the multiplexed device chip containing four fully functional microreactors. (c) Enlarged view of one of the microreactor with WE, RE, and CE cells separated by diffusion barriers. The area of WE is ∼0.3 mm^2, and the width and height of the diffusion barriers are 25 and 7.3 μm, respectively. The total volume of each cell is ∼9 nL. The collection area determined from the microscope is represented as a green spot of ∼50 μm on the WE. (d) Schematic representation of the microfluidic platform in (i) closed and (ii) open positions with a movable optical setup on top. (e) 3D view of the microfluidic platform along with the photographic image on left.

An alternative approach to generate acid locally is the use of electrochemical redox processes involving proton exchange reactions. Southern and Egeland[15] reported a device consisting of a reaction chamber containing an array of microelectrodes on a glass substrate with an electrolyte containing redox-active molecules that exchanged protons with the electrolyte. When a current was applied to the microelectrodes, acid was generated in close proximity to them. However, the fast diffusion of protons limited the range of acidity and the contrast between the different spots to achieve high reaction yields.[16] To avoid the diffusion of the protons, the local control of acidity was improved by implementing a porous substrate on the electrodes and scavenging molecules in the electrolyte.[17] The reactions were confined inside the porous substrate near the electrodes, and the protons were annihilated outside. Regardless of the improvement achieved using this method in the local control of acidity, the acidity range was too low to achieve high yields. Recently, we reported a device to control acidity in nanoliter volumes using a platform that consisted of an electrochemical cell with working, counter, and reference electrodes separated by long channels that acted as diffusion barriers.[18] The barriers were designed to avoid the reduction of protons at the counter electrode and to confine the proton concentration in the working electrode cell. Using polymerized 4-aminothiolphenol (ATP) as redox-active molecules functionalized on the electrode surface, an applied current generated acid through the oxidation reaction. We reported binary actuation of the pH in a range from 7 to 1, the stability of the attained pH for longer than 15 min, and the reversibility of the oxidation and reduction reactions.

Here, we present miniaturization of a device able to produce large acidity contrasts in confined microreactors and maintain it for times much longer than what the diffusion of the protons in free space would allow. The new device contains four electrochemical cells with each containing working, reference, and counter electrode cells separated by diffusion barriers. The miniaturized reactors use less than 2.5 nL volumes in an area of ∼0.3 mm^2. In addition to the binary mode of pH actuation from 7 to 2.6, we also show the quantitative control of pH with an accuracy of ∼0.4 pH units. Furthermore, the multiplexed control of acidity in two of the reactors showing contrast pH changes is presented. The performance of the device in terms of the reversibility of acidity control and the stability of attained pH is also reported.

2. MATERIALS AND METHODS

2.1. Fabrication of the Chip. The chip was fabricated using optical lithography. A maskless aligner MLA 150 from Heidelberg Instruments was used to pattern the designs. The series of experimental steps involved in the fabrication process is detailed in the Supporting Information (SI). Briefly, the substrate was spin-coated with an optical resist, and the design of electrodes with contact pads was exposed and developed. Later, 5 nm of titanium and 50 nm of gold were evaporated using an e-beam evaporator. The chip was placed in acetone for lift-off. Then the chip was spin-coated with an SU8 3010 epoxy resist to make the second layer. The chip was afterward

https://doi.org/10.1021/acsomega.2c06897
ACS Omega 2023, 8, 7587−7594

developed and hard baked for 10 min. The area of the electrodes was further increased by electrochemical platinization. The chip was later activated in a UV ozone cleaner for 30 min and functionalized with 0.5 mM concentration of ATP in absolute ethanol for 24 h. Other details of fabrication are explained in the SI Figure SI-1.

2.2. Electropolymerization and Acidity Control on the Platform. The cell was placed in an open position and the electrodes were connected to a potentiostat channel (Pstat 1) with the traditional three-electrode configuration for cyclic voltammetry. A cyclic voltammetry program was applied in the range of −0.25 to +0.7 V at a scan rate of 50 mV/s for three cycles in the presence of a fluorescence label carboxy seminapthorhodafluor (cSNARF) (0.5 μM) solution in KCl (1 M).

The effect of the scan rate was investigated to determine the best electrochemical conditions for the pH control. Multiplexing experiments were performed in the cell closed position with the first potentiostat channel (Pstat 1) connected to cell 1 of the chip and the second potentiostat channel (Pstat 2) connected to cell 2 of the chip through a switch box. A cyclic voltammetry program was applied between −0.7 and +0.7 V versus a pseudoreference at a scan rate of 20 mV/s for 20 cycles. The microscope objective was focused on the working electrode (WE) of the cell investigated using the internal diaphragm of the microscope to limit the area of the collection region within the WE. For the multiplexing experiments, the microscope was focused on the WE of cell 2 for the cycles 1 to 5 and 11 to 15 and on the WE of cell 1 during the cycles 6 to 10 and 16 to 20.

2.3. Chemicals and Instrumentation. 4-ATP, potassium chloride (KCl), and absolute ethanol (EtOH) were purchased from Sigma-Aldrich. cSNARFs were purchased from Molecular Probes Inc. For electrolyte preparation and cleaning purposes, millipore-filtered water was used. For the electropolymerization and pH control experiments, a Solartron Modulab XM Pstat 1mS/s potentiostat (Pstat 1) was used. For the multiplexing experiments, a Gamry potentiostat REF600-05104 (Pstat 2) was used.

3. RESULTS AND DISCUSSION

3.1. Design of the Chip and Description of the Setup. Figure 1a shows the CAD designs of (i) the full chip containing the four microreactors in the center and the corresponding leads to the bondpads, (ii) an enlarged view of the center region with four microreactors and diffusion barriers, and (iii) a zoom on one of the microreactors containing three electrodes and the diffusion barrier. The design of the metal electrodes is shown in orange and the design of the SU8 region in green. Figure 1b shows the microscopy image of the center part of one of the fabricated chips that includes four microreactors and an enlarged view of one of them showing a WE, a counter electrode (CE), and a reference electrode (RE), which are confined in each of the different cells by the lithographed epoxy. The working principle of each miniaturized cell is similar to the one we showed in a previous work with macroscopic cells.[18] To summarize the operating principle, the long channels separating WE from the CE and RE act as diffusion barriers to keep the generated protons in the WE partial cell. To generate hydrogen ions, the electrodes are functionalized with 4ATP. After the polymerization process of the molecules on Pt, they dimerize to a redox-active molecular state with two benzene rings having one amino group each,[19] which at low applied voltages reversibly exchanges protons with the solution thereby changing the pH locally on each of the electrode cell, with quasi-reversible redox reactions.

$$\mathrm{Pt{-}S{-}C_6H_4{-}NH{-}C_6H_4{-}NH_2} + 2e^- \leftrightarrow \mathrm{Pt{-}S{-}C_6H_4{-}N{=}C_6H_4{=}NH} + 2H^+ \quad (1)$$

During oxidation (left to right in eq 1), two electrons are required to generate two protons, while in the reverse part of the cycle (right to left in eq 1), the retake of protons from the solution by a reduction reaction consumes two electrons. In the CE, the opposite reaction to the WE equilibrates the charge balance during the whole process.

The long separating channels avoid the reduction of protons at the CE, enabling the increase of local acidity. To compute proton diffusion along the channel, we used a one-dimensional model, keeping in mind that the volume of the channel had to be significantly smaller than the volume of the electrode cells in order to avoid the influence of the channel in each microvessel during proton diffusion. In the one-dimensional model, the diffusion time of the protons τ can be calculated from the length of the barrier L and diffusion constant of protons ($D = 9 \times 10^{-5}$ cm^2/s) as $\tau = L^2/\pi^2 D$.[20] Our channel length of ∼0.8 cm was designed to provide a diffusion time of 11 min for the protons to reach the CE. The width and the height of the barrier were ∼25 and ∼7.2 μm, respectively. The volume of the electrode cell was ∼2.5 nL.

Different identical chips were fabricated and each chip was mounted on our in-house-made microfluidic platform as schematically shown in Figure 1d (including the optical setup in (i)). The top component of the microfluidic platform contains an optical window, a microfluidic inlet and an outlet, and electrical contacts that connect the chip to an external switch box, which also connects to the potentiostat channels. The bottom part also includes a movable piston that allows to move the chip up and down to close and open the cell. The chip was sealed with an O-ring that isolates the liquid from the contact pads. When the platform is closed actuating the piston, the glass window from the top comes in contact with the epoxy barriers on the chip, isolating the electrode cells and channels (as shown in gray in Figure 1d(i)). If the piston is lowered, the cell is in the open position (Figure 1d(ii)) allowing to exchange and flush new electrolytes. The platform was placed under an optical microscope Olympus BX customized setup that uses an LED source centered at 580 nm (CoolLED-pE4000). The changes in fluorescence were monitored using the fluorescence marker cSNARFs through a 20× objective, and the illuminated area was limited by a diaphragm to a field of view of ∼50 μm (represented in Figure 1c with the green spot). We used 1 M concentration of KCl solution with 0.5 μM cSNARF as the electrolyte. For pH control measurements, the microscope objective could be moved to the respective electrode cells of the different microreactors and the focus was adjusted to obtain the maximum fluorescence. Figure 1e shows the 3D view of the microfluidic platform along with the photograph of the platform under the microscope. On the present chip design, we used a circular arrangement of electrodes and channels at the center so that they occupy most of the flat available surface of the spin-coated resist. Additionally, the concentric arrangement of channels could relax the tension producing less cracks on the processed samples.

https://doi.org/10.1021/acsomega.2c06897
ACS Omega 2023, 8, 7587−7594

3.2. Control of Acidity in One Microreactor. The acidity in the cells was controlled by the reversible redox reactions of 4ATP that exchange protons with the electrolyte. The redox-active states of 4ATP were created by polymerizing electrochemically the self-assembled monolayer[21] with the chip in the open position to reduce the external resistivity existing when the electrodes are connected only through the diffusion barriers (closed cell configuration). Following the electropolymerization, the platform was flushed with a fresh electrolyte and placed in a closed position to constrain the volume for pH control measurements. Each reactor was connected to the potentiostat with a three-electrode configuration using WE, CE, and RE as shown in Figure 1c. Cyclic voltammetry (CV) was used to drive the redox reactions on the polymerized 4ATP layer. The microscope was focused on the WE to monitor the acidity changes through the fluorescence spectrum during CV measurements. The pH inside the electrode cell was monitored by the SNARF signal, which has two peaks, one at 590 nm that is dominant under more acidic pH and the other at 655 nm that is dominant under more alkaline pH. The relative intensity of the two peaks can be used to calibrate the pH. We used an excitation wavelength at 565 nm close to the absorbance of the SNARF molecule that provided the highest intensity. To avoid stray light, we used a filter at 590 nm. The calibration of the fluorescence at 655 nm normalized to the initial pH 7.4 peak intensity is shown in Figure SI-3. The initial pH in the experiment was calibrated using the relative intensity of both peaks at 590 and 650 nm; then, we followed the pH variations with the intensity of the peak of SNARF at 655 nm normalized to the initial value with the fresh electrolyte at pH 7.4. Each point was integrated for 1 s during the CV.

Figure 2a–c shows the bias voltage, the corresponding current, and the 655 nm peak fluorescence normalized to the peak intensity at pH 7.4, respectively, plotted against time during 5 cycles. The voltage was biased between −0.75 and +0.75 V at a rate of 50 mV/s. The sweep from 0 to 0.5 V gives rise to an oxidation peak as shown in Figure 2d, which corresponds to the gray shaded region shown in the second cycle of Figure 2b. Following the oxidation, a decrease in the fluorescence intensity is observed (Figure 2c), which marks the decrease of the pH in the cell. The voltage sweep from 0 to −0.5 V produces a reduction peak as shown in the region shaded in blue in Figure 2b, followed by an increase in the fluorescence intensity observed in (c) indicating that the neutral pH was recovered. This cycle was repeated successively showing reversible changes on the fluorescence intensity driven by the reversible redox states of the 4ATP molecule that releases protons during the oxidation reaction and recovers them from the electrolyte during the reduction reaction thereby controlling the acidity in the WE cell. In Figure 2b, we also observed a small peak before the main oxidation, which was detected in the successive cycles. The origin of this oxidation peak at lower energies is attributed to the oxidation of 4ATP on remaining Au having slightly different potentials to the 4ATP on Pt, as we observed only in some samples where the electrodes were not completely platinized. In Figure 2e, we show the SNARF fluorescence spectra corresponding to cycle 2 (shaded region in (b)) where the spectrum from the oxidation peak of 4ATP is denoted in gray and that from the reduction peak is denoted in blue. For a pH value less than 5, the SNARF peak at 655 nm completely quenches and the lower pH is beyond the measurable range. The minimum pH

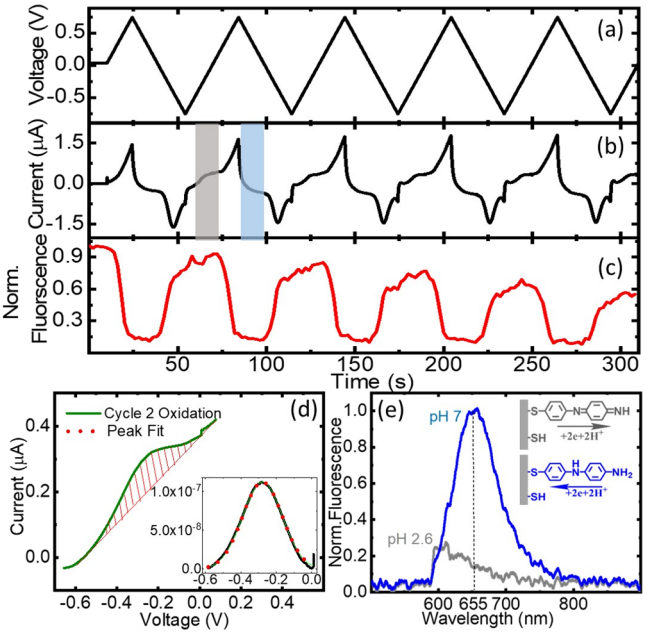

Figure 2. Graph showing (a) voltage, (b) current, and (c) normalized intensity of the fluorescence marker plotted against time. (d) Current is plotted against voltage for cycle 2 (data correspond to the shaded region in panel (b)). The inset shows the Gaussian fitting of the peak in red, and the subtracted data of current versus voltage are shown in black. (e) SNARF fluorescence spectrum showing the maximum and minimum intensity peaks corresponding to the pH values of 7 and 2.6, respectively. Schematic representation of the oxidation (in gray) and reduction (blue) reactions of the 4ATP molecules is shown in the right corner.

beyond the range of the SNARF marker (Figure 2e) could be then estimated by calculating the total charge exchanged by the electrons in the cell (Q) and attributing that charge exchange to redox reactions producing only protons. As the pH change is more than two units, as monitored by SNARF, the final concentration exceeds largely the initial one at neutral pH, and the measuring time is much smaller than the diffusion time of protons through the diffusion barriers. The pH was calculated by converting Q into the number of protons and retrieving the concentration using the volume in the cell:

$$\mathrm{pH} = -\log\left[\frac{Q}{F \times V_{\mathrm{cell}}}\right] \tag{2}$$

where F is the Faraday constant and V_{cell} is the volume of the WE cell (~2.5 nL). The charge Q was obtained from the integrated area under the oxidation peak and the scan rate υ

$$Q = \int {}^{I}/_{\upsilon}\, dt \tag{3}$$

In Figure 2d, the oxidation peak for cycle 2 indicating the area under the peak (shaded region in Figure 2b) is shown along with the inset presenting the Gaussian fitting, and the results from the fitting are tabulated in Table 1. The minimum pH attained in the cell resulting from eq 1 was calculated as 2.6 (we have verified this procedure with a recent article where we

Table 1. Gaussian Fitting and the Results from the Fitting

peak type	peak area (C)	max height (A)	FWHM (V)
Gaussian	6.32×10^{-7}	1.12×10^{-7}	0.27

https://doi.org/10.1021/acsomega.2c06897
ACS Omega 2023, 8, 7587−7594

linked the faradaic currents with the pH using a different pH marker[22]).

3.3. Quantitative Control and Retention Time of the Acidity. An accurate control of the acidity in the cell can be used to manage different chemical reactions that can be activated with different pH values, for example, to protect sidechains of biopolymers, while targeting a main chemical group. In our device, we tested to quantitatively control the acidity by using pulse voltammetry. Figure 3a,b shows the

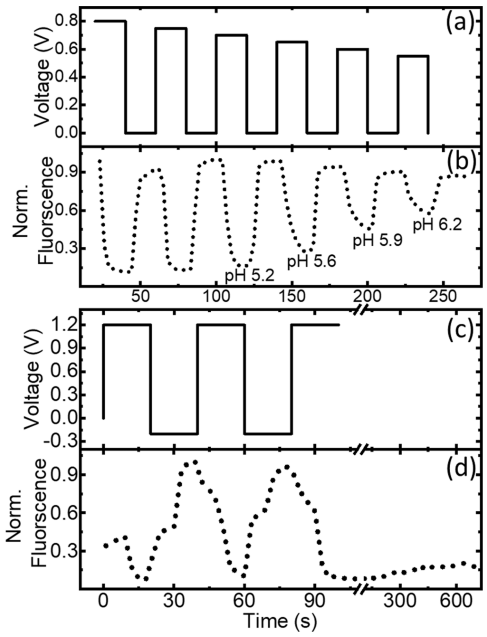

Figure 3. Graph showing (a) the voltage pulse and (b) the corresponding fluorescence spectra with different pH values plotted against time. The graph shows the voltage pulse (c) and the corresponding fluorescence spectra plotted against time (d).

applied voltage and the recorded fluorescence, respectively. Different voltages with pulses of 20 s were applied while monitoring the pH through the fluorescence intensity (Figure 3a). Using a pulse of 0.8 V, we were able to quench the fluorescence and bring the pH below 5. We waited for an equivalent time of 20 s that allowed the stabilization of the pH in the cell. In the following pulses, we decreased the amplitude in steps of 0.05 V until reaching 0.55 V. The fluorescence was also quenched during the second pulse at 0.75 V, indicating that the pH was still below 5. For the next voltage pulse at 0.7 V, the fluorescence intensity was slightly higher than that of the previous pulse. At 0.65 V, the intensity was higher than the previous pulse and this process was repeated for the next consecutive pulses. The corresponding pH values for the fluorescence extracted from the calibration plot (SI Figure SI-3) as denoted in Figure 3b indicated that in addition to the binary mode of pH actuation, we were able to regulate the acidity by ΔpH of ∼0.3 units.

We also tested the stability in terms of retention time of the attained pH in the electrode cell: after applying voltage pulses of 20 s from −0.15 to 1.2 V for three cycles to stabilize the system with the reversible pH transitions, we opened the circuit in the acidic range of equilibrium at 1.2 V while monitoring the pH with the fluorescence for more than 10 min. Figure 3a shows the voltage pulses, and Figure 3b shows the fluorescence spectra plotted against time. A break is introduced after 100 s until before 200 s where the fluorescence was constant (full graph is shown in the SI, Section D). Until 300 s (5 min), we observed no noticeable change in the fluorescence intensity. This time is already quite larger than the diffusion time to cover the distance between both partial cells of the WE and CE in the absence of diffusion barriers. After 5 min, a slight increase in the intensity was observed. At 600 s (10 min), the fluorescence intensity was 0.17 and from the calibration plot (Figure SI-3), the pH maintained in the cell was below the SNARF detection range, which is at pH 5. These measurements show that the design of the device along with the model of the diffusion barrier enables the miniaturization. Furthermore, the ability to sustain the acidic conditions for 5 min already opens up applications that control different chemical processes.

3.4. Reversibility Tested over 100 Cycles. We studied the reversibility of acid control driving CVs over 100 cycles while monitoring the fluorescence. The voltage was adjusted from −0.6 to 0.7 V using a scan rate of 100 mV/s. The fluorescence spectra were recorded with integration times of 1 s each. Figure 4a shows the spectra corresponding to cycles 2

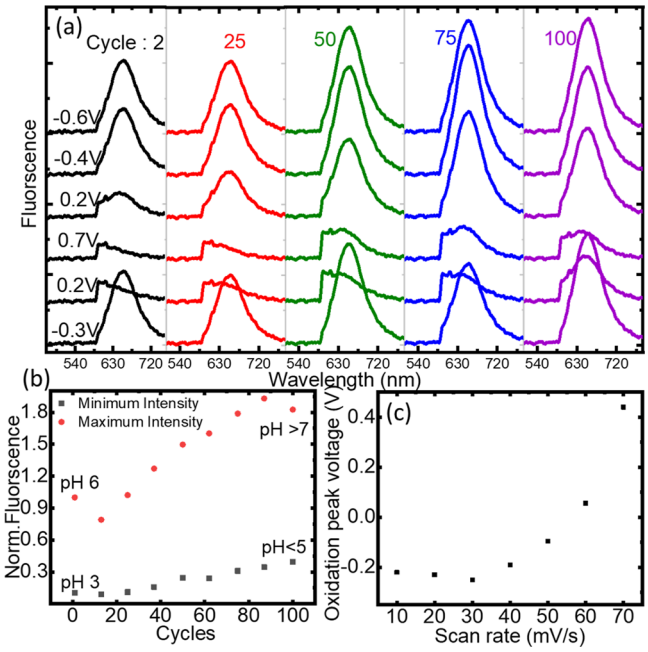

Figure 4. (a) SNARF fluorescence spectra plotted for the CV cycles 2, 25, 50, 75, and 100 in a voltage range from −0.75 to +0.75 V with an offset in the *Y* axis. (b) Plot of the CV cycles against the normalized fluorescence intensity of the SNARF spectra indicating the maximum and minimum intensities. (c) Scan rate plotted against the voltage at the oxidation peak.

(black), 25 (red), 50 (green), 75 (blue), and 100 (purple) extracted at different voltages to illustrate the fluorescence behavior. The spectra are plotted with a vertical offset showing a part of the baseline for reference, while the relative scale is constant to enable comparison among them. The spectra repeated the expected behavior of pH already explained depending on the oxidation/reduction of 4ATP. Initially, in cycle 2 (in black), during the voltage sweep at −0.6 V (top spectrum), the fluorescence peak at 655 nm corresponds to the neutral pH in the electrode cell. Toward positive voltages around 0.7 V (fourth spectrum), the 655 nm peak was quenched due to the increase of acidity made by 4ATP

https://doi.org/10.1021/acsomega.2c06897
ACS Omega 2023, 8, 7587−7594

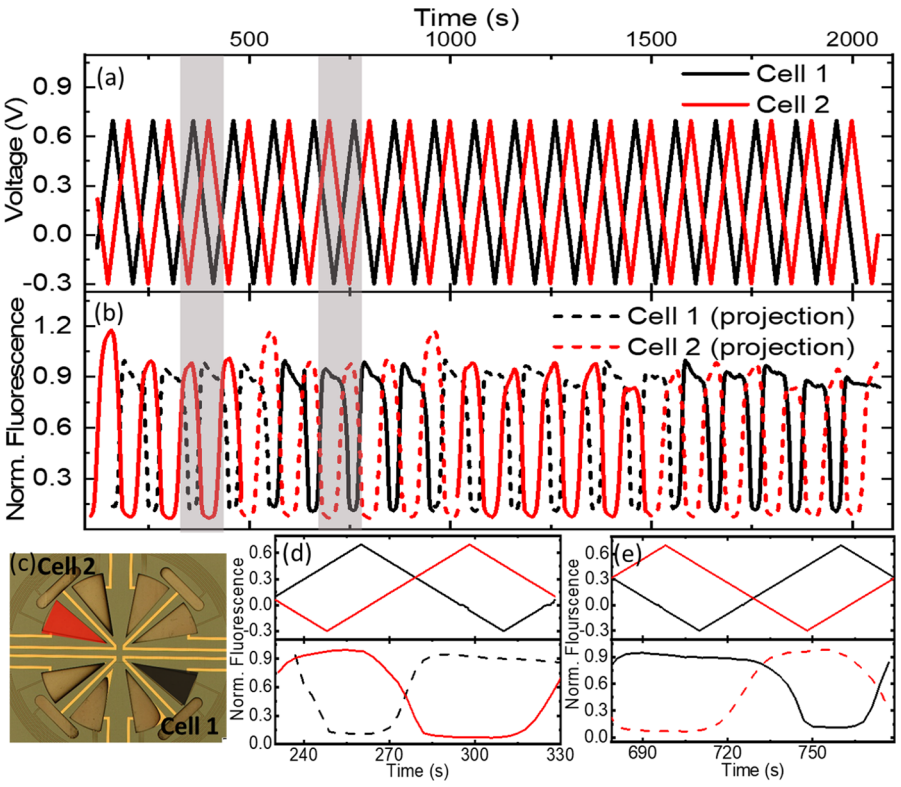

Figure 5. Multiplexed control of acidity in cell 1 and cell 2. (a) The voltage applied in cell 1 and cell 2 is shown in black and red, respectively, and (b) the corresponding fluorescence spectra are plotted against time. The dotted plots of cell 1 and cell 2 represent the projection of the spectra. (c) Microscopy image of the chip highlighting the WE of cell 1 and cell 2. (d,e) Enlarged view of the shaded area in panels (a,b).

oxidation and at −0.3 V (bottom spectrum), the increase in peak intensity witnesses the recovery of more basic conditions. A similar behavior in each of the cycles was observed as shown in the examples of cycles 2, 25, 50, 75, and 100, where the peak at 655 nm appeared and quenched indicating neutral and acidic pH conditions in the cell, respectively.

Figure 4b shows the cycle dependence of the maxima and minima peak intensities on the fluorescence plotted in red and black, respectively. Until 25 cycles, we observe a slight decrease of the fluorescence associated with an increase of acidity, both for the acidic part of the cycle and the alkaline part of the cycle, which indicates that more protons are being produced in the first cycle. After 25 cycles (40 min), we observed an increase of both intensities, which reflects a rise in the overall alkalinity of the system. Some values corresponding to the reduction part of the CV even had fluorescence over 1.8 with respect to the initial fluorescence, which corresponds to alkaline values well above the initial neutral pH. The progressive increase of alkalinity in the system after 25 cycles could be attributed to the loss of protons due to leakages and/or to gaps in the 4ATP functionalization at the electrode surface, which would result in sites where direct exchange of electrons with protons would reduce them into hydrogen gas (H_2) during the negative voltage bias. Both effects can decrease the overall proton concentration in the cells resulting in an increase in the basicity in the microreactor. Nevertheless, the minimum pH attained in the cell after 100 cycles was still under 5 from our calibration. The acidity of the system could be recovered after flushing the cell with a fresh electrolyte (we show data of regeneration in the SI with an experiment where we tested 1000 cycles, Section E Figure SI-4).

The kinetics of the redox reactions was also tested with CV cycles at different scan rates from 10 to 70 mV/s. In Figure 4c, the scan rate is plotted against the voltage at the oxidation peak. We observed a shift in the oxidation peak potential from 0.2 to 0.4 V when the scan rate was increased from −30 to 70 mV/s, respectively. This increase occurs because higher rates do not allow the 4ATP molecule oxidation reaction to occur on time, and thus the protons were not fully exchanged at their normal value and continued to exchange after surpassing the peak. The control of the acidity can be performed with lower rates until 30 mV/s; however, at higher scan rates, the applied voltage has to increase, which affects the reversibility to control many cycles.

3.5. Multiplexed Control of Acidity in Two Cells with Different Phases. Chips with multiple cells were designed to allow simultaneous control of acidity in different cells. To control this feature, two channels of the potentiostat were connected and we adjusted the CV cycles to apply the voltage out of phase introducing a delay time at the start of the CV of channel 2. We used a voltage range of −0.3 to 0.7 V at a scan rate of 20 mV/s in both channels. To measure the fluorescence signal in each cell using our single-channel spectrometer, we alternated the position of the microscope spot between two cells every five cycles to complete 20 cycles. This was possible due to the good planarity of our system that allowed to go from one cell to the next one without losing focus. Figure 6 shows the applied voltage and the corresponding fluorescence intensity plotted against time in cells 1 and 2 in black and red, respectively. The WE cells 1 and 2 are shaded in black and red, respectively, in Figure 5c. To visualize the behavior of acidity, the data from the previous five cycles of the two cells were projected in dotted lines for the cycles where the microscope

https://doi.org/10.1021/acsomega.2c06897
ACS Omega 2023, 8, 7587−7594

objective was on the other cell since simultaneous measurement of the fluorescence intensity in the two cells was not possible. Both cells 1 and 2 (plotted in black and red, respectively) show the behavior already described with oxidation and reduction at ∼0.7 and 0. 1 V, respectively, and the fluorescence follows the acidic behavior of the redox reactions. The fluorescence is shown to be out of phase on both cells, following the respective bias actuation. It is also remarkable that the projected fluorescence plotted in dotted lines for both cells shows very good continuity with the real fluorescence, which indicates that during the time when the fluorescence is not monitored in each cell, the acidity follows the expected behavior. The enlarged views of the CV cycles in the shaded areas in Figure 5a,b are shown in (d) and (e), respectively. The changes in the fluorescence intensity with respect to the applied voltage bias could be seen along with the contrast fluorescence changes in the other cell, which are denoted as a projection. For 20 cycles, alternating pH conditions of acidic—neutral were demonstrated in cell 1 and cell 2 maintaining the contrast conditions. As conclusion, we conducted the multiplexed control of acidity in these two miniaturized cells in an independent way.

3.6. Simultaneous Control of Acidity in Two Cells. An additional test was performed to verify the possibility to control two microreactors simultaneously using the same potentiostat. The experiment recorded the CV of cell A and B separately (red and black curves, respectively, in Figure 6)

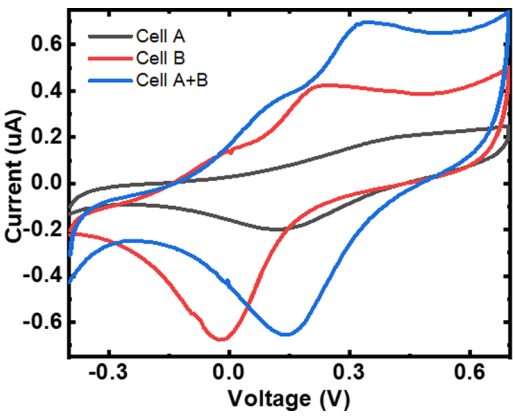

Figure 6. CV curves for cell A and cell B (black and red, respectively) and the multiplexed CV of both cell A and cell B in short circuit.

from −0.4 to 0.7 V at a scan rate of 20 mV/s and comparing the currents when shortcutting WE, CE, and RE of both microreactors (shown in blue). The CV of the shorted electrodes showed the sum of the faradaic currents from both cells indicating that each WE worked on its own without potential leakage and confirmed the ability of the system to perform experiments in parallel.

4. CONCLUSIONS AND OUTLOOK

We fabricated a miniaturized device with four microreactors to control the acidity in miniaturized regions. The control of pH was demonstrated using the electrochemical reactions of redox-active 4ATP derivatives functionalized on the surface of the electrodes. The microreactor was designed to confine the protons in electrode cells, while the reduction of protons at the electrodes was avoided using diffusion barriers separating the WE and CE. A fluorescence marker in the electrolyte was used to track the pH. We were able to control the acidity in the individual microreactor from pH 7 to complete quenching of the marker at 5. The minimum pH attained in the cell was 2.6 as was calculated from the charge transfer of the polymerized 4ATP molecules. We demonstrated that regardless of the miniaturization, the pH was controlled similarly to the rules described in a previous article with a reactor of 1 cm diameter, which demonstrates that the acidity control is independent of the footprint of the microreactors. Further miniaturization of the device would be possible thanks to our design. We showed a quantitative control of pH with an accuracy of ∼0.4 pH units by varying the amplitude of the applied potential pulses. The microreactor retains a stable pH in the electrode cell for 10 min by the confinement of protons, thanks to the tailored diffusion barriers. This time control would allow to drive chemical reactions such as synthesis of biopolymers that we expect to occur faster than in macroscopic vessels because the diffusion of reagents within this cell is limited with the miniaturized volumes. The reversibility of the acidity control was tested over 100 cycles. The minimum pH corresponding to the 100th cycle was still less than 5. This shows that the system has good control over the reversibility providing a dynamic acidity control and is well suited for combinatorial chemistry applications. For example, one of the current challenges of combinatorial chemistry is peptide synthesis. Current methods use 50% concentration of trifluoracetic acid to remove the protecting groups in macroscale reactors. The pH corresponding to this concentration is ∼5.9 (more information is provided in the SI). As the generation of acid through the redox reactions of ATP also occurs in organic solvents,[23] our device has the potential to implement electrochemically controlled synthesis. The multiplexed control of acidity was demonstrated in two cells on the same chip using simultaneous CV measurements that are out of phase to maintain different pH values without any crosstalk. This shows that our device could be used for combinatorial chemistry applications where the regulation of the large acidity range would enhance the throughput and the yield of chemical reactions.

In summary, we have demonstrated to the best of our knowledge the largest control of acidity in terms of acidity range and retention time driven by electrochemical means in cells miniaturized in the range of 100 μm. We also showed that the pH could be independently activated in different cells. We believe that the key features of our device's large pH range, quantitative control, reversibility, and multiplexing could be used to control chemical reactions with increased throughput assuring stability of acid contrast between nearby spots.

■ ASSOCIATED CONTENT

Supporting Information

The Supporting Information is available free of charge at https://pubs.acs.org/doi/10.1021/acsomega.2c06897.

Design and fabrication steps of the electrochemical chip including pH calibration of the fluorescence marker, additional details about the experiments of electropolymerization, retention time of acidity in the microreactor, and recovery of acidity control after 1000 CV cycles, and calculation of the proton concentrations in organic solvents (PDF)

https://doi.org/10.1021/acsomega.2c06897
ACS Omega 2023, 8, 7587−7594

AUTHOR INFORMATION

Corresponding Author

César Pascual García − *Luxembourg Institute of Science and Technology (LIST), L-4422 Belvaux, Luxembourg;* orcid.org/0000-0002-0526-2507; Email: cesar.pascual@list.lu

Authors

Divya Balakrishnan − *Luxembourg Institute of Science and Technology (LIST), L-4422 Belvaux, Luxembourg;* orcid.org/0000-0001-5540-4633

Janwa El Maiss − *Luxembourg Institute of Science and Technology (LIST), L-4422 Belvaux, Luxembourg*

Wouter Olthuis − *MESA+ Institute, University of Twente, 7522 NB Enschede, Netherlands;* orcid.org/0000-0002-7018-1383

Complete contact information is available at: https://pubs.acs.org/10.1021/acsomega.2c06897

Author Contributions

The manuscript was written through contributions of all authors. All authors have given approval to the final version of the manuscript.

Notes

The authors declare no competing financial interest.

ACKNOWLEDGMENTS

This research work was financed by the FNR ATTRACT project 5718158 NANOpH, and from the program H2020 Future Emerging Technlogies of the European Comission under the grant No 862539- Electromed-FET-Open. We would like to thank Mathieu Gerard for his contribution in the cover design by providing us the technical drawings of the sensors.

REFERENCES

(1) Elbaz, J.; Wang, Z. G.; Orbach, R.; Willner, L. PH-Stimulated Concurrent Mechanical Activation of Two DNA "Tweezers". A "SET-RESET" Logic Gate System. *Nano Lett.* **2009**, *9*, 4510−4514.

(2) Idili, A.; Vallée-Bélisle, A.; Ricci, F. Programmable PH-Triggered DNA Nanoswitches. *J. Am. Chem. Soc.* **2014**, *136*, 5836−5839.

(3) Mattath, M. N.; Ghosh, D.; Pratihar, S.; Shi, S.; Govindaraju, T. Nucleic Acid Architectonics for PH-Responsive DNA Systems and Devices. *ACS Omega* **2022**, *7*, 3167−3176.

(4) Ye, C.; Cao, H. H.; Zhang, R. R. Selective Assembly of DNA Nanocages Controlled by PH/Annealing. *Xiandai Huagong/Modern Chem. Ind.* **2020**, *40*, 179−183.

(5) Gordon, C. K. L.; Eisenstein, M.; Soh, H. T. Direct Selection Strategy for Isolating Aptamers with PH-Sensitive Binding Activity. *ACS Sens.* **2018**, *3*, 2574−2580.

(6) Abaci, U.; Ustalar, A.; Yilmaz, M.; Guney, H. Y. Synthesis of New 2,5-Di(Thiophen-2-Yl)Furan-3-Carbonitrile Derivatives and Investigation of the Electrochromic Properties of Homopolymers and Co-Polymers with EDOT. *RSC Adv.* **2016**, *6*, 27836−27845.

(7) Palomo, J. M. Solid-Phase Peptide Synthesis: An Overview Focused on the Preparation of Biologically Relevant Peptides. *RSC Adv.* **2014**, *4*, 32658−32672.

(8) Amodio, A.; Adedeji, A. F.; Castronovo, M.; Franco, E.; Ricci, F. PH-Controlled Assembly of DNA Tiles. *J. Am. Chem. Soc.* **2016**, *138*, 12735−12738.

(9) Müller, M. M.; Muir, T. W. Histones: At the Crossroads of Peptide and Protein Chemistry. *Chem. Rev.* **2015**, *115*, 2296−2349.

(10) Okochi, M.; Muto, M.; Yanai, K.; Tanaka, M.; Onodera, T.; Wang, J.; Ueda, H.; Toko, K. Array-Based Rational Design of Short Peptide Probe-Derived from an Anti-TNT Monoclonal Antibody. *ACS Comb. Sci.* **2017**, *19*, 625−632.

(11) De-Simone, S. G.; Napoleão-Pêgo, P.; De-Simone, T. S. Spot Synthesis: An Optimized Microarray to Detect Ige Epitopes. *Methods Mol. Biol.* **2016**, *1352*, 263−277.

(12) Yu, J.; Tangsombatvisit, S.; Levy, D.; Varma, M.; Xu, G.; Utz, P. J.; Price, J. V.; Liu, C. L.; Gozani, O.; Baechler, E. C. On Silico Peptide Microarrays for High-Resolution Mapping of Antibody Epitopes and Diverse Protein-Protein Interactions. *Nat. Med.* **2012**, *18*, 1434−1440.

(13) Gao, X.; LeProust, E.; Zhang, H.; Srivannavit, O.; Gulari, E.; Yu, P.; Nishiguchi, C.; Xiang, Q.; Zhou, X. A Flexible Light-Directed DNA Chip Synthesis Gated by Deprotection Using Solution Photogenerated Acids. *Nucleic Acids Res.* **2001**, *29*, 4744−4750.

(14) Elbaz, J.; Wang, F.; Remacle, F.; Willner, I. PH-Programmable DNA Logic Arrays Powered by Modular DNAzyme Libraries. *Nano Lett.* **2012**, *12*, 6049−6054.

(15) Egeland, R. D.; Southern, E. M. Electrochemically Directed Synthesis of Oligonucleotides for DNA Microarray Fabrication. *Nucleic Acids Res.* **2005**, *33*, No. e125.

(16) Maurer, K.; McShea, A.; Strathmann, M.; Dill, K. The Removal of the t -BOC Group by Electrochemically Generated Acid and Use of an Addressable Electrode Array for Peptide Synthesis. *J. Comb. Chem.* **2005**, *7*, 637−640.

(17) Maurer, K.; Cooper, J.; Caraballo, M.; Crye, J.; Suciu, D.; Ghindilis, A.; Leonetti, J. A.; Wang, W.; Rossi, F. M.; Stöver, A.G.; et al. Electrochemically Generated Acid and Its Containment to 100 Micron Reaction Areas for the Production of DNA Microarrays. *PLoS One* **2006**, *1*, No. e34.

(18) Balakrishnan, D.; Thomann, J. S.; Lamblin, G.; van den Berg, A.; Olthuis, W.; Pascual-García, C. Electrochemical Control of PH in Nanoliter Volumes. *Nano Lett.* **2018**, *18*, 2807−2815.

(19) Hayes, W. A.; Shannon, C. Electrochemistry of Surface-Confined Mixed Monolayers of 4-Aminothiophenol and Thiophenol on Au. *Langmuir* **1996**, *12*, 3688−3694.

(20) Clément, N.; Nishiguchi, K.; Dufreche, J. F.; Guerin, D.; Fujiwara, A.; Vuillaume, D. Water Electrolysis and Energy Harvesting with Zero-Dimensional Ion-Sensitive Field-Effect Transistors. *Nano Lett.* **2013**, *13*, 3903−3908.

(21) Balakrishnan, D.; Lamblin, G.; Thomann, J. S.; Guillot, J.; Duday, D.; Van den Berg, A.; Olthuis, W.; Pascual-García, C. Influence of Polymerisation on the Reversibility of Low-Energy Proton Exchange Reactions by Para-Aminothiolphenol. *Sci. Rep.* **2017**, *7*, 15401.

(22) El Maiss, J.; Balakrishnan, D.; Pascual García, C.*Universal Control of Protons Concentration Using Electrochemically Generated Acid Compatible with Miniaturization*; 2022.

(23) El Maiss, J.; Balakrishnan, D.; García, C. P. Universal Control of Proton Concentration Using an Electrochemically Generated Acid Compatible with Miniaturization. *Nanoscale Adv.* **2022**, *4*, 3233.